Journal of
Low Power Electronics and Applications

MDPI

Article

Spin–Orbit Coupling Free Nonlinear Spin Hall Effect in a Triangle-Unit Collinear Antiferromagnet with Magnetic Toroidal Dipole

Satoru Hayami

Graduate School of Science, Hokkaido University, Sapporo 060-0810, Japan; hayami@phys.sci.hokudai.ac.jp

Abstract: We investigate emergent conductive phenomena triggered by collinear antiferromagnetic orderings. We show that an up-down-zero spin configuration in a triangle cluster leads to linear and nonlinear spin conductivities even without the relativistic spin–orbit coupling; the linear spin conductivity is Drude-type, while the nonlinear spin conductivity has Hall-type characterization. We demonstrate the emergence of both spin conductivities in a breathing kagome system consisting of a triangle cluster. The nonlinear spin conductivity becomes larger than the linear one when the Fermi level lies near the region where a small partial band gap opens. Our results indicate that collinear antiferromagnets with triangular geometry give rise to rich spin conductive phenomena.

Keywords: nonlinear spin Hall effect; triangular lattice; magnetic toroidal moment; spin–orbit coupling; multipole; tight-binding model

check for updates

Citation: Hayami, S. Spin–Orbit Coupling Free Nonlinear Spin Hall Effect in a Triangle-Unit Collinear Antiferromagnet with Magnetic Toroidal Dipole. *J. Low Power Electron. Appl.* **2024**, *14*, 35. https://doi.org/10.3390/jlpea14030035

Academic Editors: Weigang Wang and Guozhong Xing

Received: 2 June 2024
Revised: 1 July 2024
Accepted: 2 July 2024
Published: 3 July 2024

1. Introduction

Antiferromagnetic orderings and their related physical phenomena have been long studied in condensed matter physics [1–4]. Depending on spin patterns under lattice structures, a variety of symmetry lowerings are caused by antiferromagnetic phase transition. Based on Neumann's principle that connects symmetry and the appearance of physical phenomena, functional materials have been discovered. One of the examples of this is a multiferroic property produced as a consequence of both spatial inversion and time-reversal symmetry breakings, which results in a linear magnetoelectric effect caused by the coupling between electric and magnetic degrees of freedom [5–11]. Another example is the anomalous Hall effect without net magnetization when the time-reversal symmetry and other crystal symmetries are broken, meaning that the antiferromagnetic structure belongs to the same irreducible representation as the ferromagnetic state [12–21]. Complicated noncollinear/noncoplanar antiferromagnetic structures have often been studied as the origin of these physical phenomena, since they lead to a lowering of crystal symmetry.

Meanwhile, collinear antiferromagnetic structures can also lead to the same physical phenomena through a consideration of the lattice structures with multiple sublattices. For example, the multiferroic property can be engineered by staggered collinear antiferromagnetic orderings on the one-dimensional zigzag chain [22–29], two-dimensional honeycomb structure [30–34], and three-dimensional diamond structure [35–40]. In addition, the anomalous Hall effect is also induced in collinear antiferromagnets [41–49]. Since the amount of material with collinear antiferromagnetic structures is larger than that with noncollinear/noncoplanar ones, it is desirable to further explore functionalities in collinear antiferromagnets from a fundamental viewpoint.

In this context, emergent spin–orbit coupling (SOC) in antiferromagnets has recently attracted growing interest in both theory and experiments [50–72], and is sometimes referred to as "altermagnetism" [73,74]. Here, collinear antiferromagnets exhibit a symmetric momentum-dependent spin-split band structure even without the relativistic SOC. Owing to the momentum dependence of the spin splitting, a directional-dependent spin current generated by an external electric field can be expected [53,75–78]. As the SOC is not necessary to generate such a spin current, this type of collinear antiferromagnet can be a potential candidate for highly efficient spintronics devices that are not limited to heavy-element materials.

In the present study, we investigate the spin current generation in SOC-free collinear antiferromagnets by focusing on the effect of cluster geometry. We show that the collinear antiferromagnetic structure in a triangle cluster gives rise to both linear and nonlinear spin conductivities owing to the lack of spatial inversion symmetry in the triangle unit, which differs from the square cluster case. We discuss their emergence from the viewpoint of group theory and cluster multipole theory. We also study the behavior of both conductivities by analyzing the tight-binding model in the breathing kagome structure formed by triangle clusters. Our results indicate that the cluster structure plays an important role in discussing the spin current generation in SOC-free antiferromagnets.

The rest of this paper is organized as follows. In Section 2, we show the relationship between collinear antiferromagnetic structures and magnetic toroidal multipoles in the square and triangle clusters. We also introduce the tight-binding model in a breathing kagome system. Then, we show the linear and nonlinear spin conductivities under the collinear antiferromagnetic ordering in Section 3. We compare the linear and nonlinear spin conductivities in Section 4. Section 5 concludes with the results of the present paper.

2. Model

2.1. Magnetic Toroidal Multipoles in a Cluster

First, let us discuss the physical properties of antiferromagnetic structures by introducing the magnetic toroidal multipole T_{lm} [79–81], which is defined as

$$T_{lm} = \sum_j \left\{ \frac{\boldsymbol{r}_j}{l+1} \times \left(\frac{2\boldsymbol{l}_j}{l+2} + \boldsymbol{\sigma}_j \right) \right\} \cdot \boldsymbol{\nabla} O_{lm}(\boldsymbol{r}_j), \tag{1}$$

where $\boldsymbol{l}_j$ and $\boldsymbol{\sigma}_j/2$ are the dimensionless orbital and spin angular-momentum operators of an electron at $\boldsymbol{r}_j$. l and m represent the azimuthal and magnetic quantum numbers, respectively. $O_{lm}(\boldsymbol{r})$ is proportional to the spherical harmonics $Y_{lm}(\hat{\boldsymbol{r}})$ as a function of angle $\hat{\boldsymbol{r}} = \boldsymbol{r}/|\boldsymbol{r}|$, $Y_{lm}(\hat{\boldsymbol{r}})$, which is given by

$$O_{lm}(\boldsymbol{r}) = \sqrt{\frac{4\pi}{2l+1}} r^l Y_{lm}^*(\hat{\boldsymbol{r}}). \tag{2}$$

The magnetic toroidal multipole T_{lm} is characterized by time-reversal-odd polar tensor; even(odd)-rank T_{lm} has even(odd) parity for spatial inversion. When Equation (1) applies to the antiferromagnetic structure, one needs to read $\boldsymbol{r}_j$ with the position of the jth atom $\boldsymbol{R}_j$ in a magnetic unit cell [19,82].

The $l = 1$ component of T_{lm} corresponds to the magnetic toroidal dipole, which appears when both the spatial inversion and time-reversal symmetries are broken. The expression of T_{1m}, i.e., $\boldsymbol{T} = (T_x, T_y, T_z)$, is proportional to $(\boldsymbol{R} \times \boldsymbol{\sigma})_j$ when the orbital angular momentum operator is neglected. Thus, the magnetic toroidal dipole $\boldsymbol{T}$ exists in the vortex-type antiferromagnetic structure; it is noted that $\boldsymbol{T}$ is also induced in the collinear antiferromagnetic structure, as shown later. When the antiferromagnetic structure induces such a magnetic toroidal dipole, the system exhibits parity-violating physical phenomena, such as the linear magnetoelectric effect [83–86] and nonreciprocal transport [27,87–90]. In particular, in the case of collinear antiferromagnets without the relativistic SOC, the nonlinear spin Hall effect can be expected in the presence of the magnetic toroidal dipole [91].

The $l = 2$ component of T_{lm} corresponds to the magnetic toroidal quadrupole, whose spatial inversion parity is $+1$, while the time-reversal parity is -1. There are five components of the magnetic toroidal quadrupole, whose expressions are given by [81]

$$T_u = 3(ZX\sigma_x - YZ\sigma_y), \tag{3}$$
$$T_v = -\sqrt{3}(ZX\sigma_y + YZ\sigma_x - XY\sigma_z), \tag{4}$$
$$T_{yz} = \sqrt{3}[-(Y^2 - Z^2)\sigma_x + XY\sigma_y - ZX\sigma_z], \tag{5}$$
$$T_{zx} = \sqrt{3}[-XY\sigma_x - (Z^2 - X^2)\sigma_y + YZ\sigma_z], \tag{6}$$
$$T_{xy} = \sqrt{3}[ZX\sigma_x - YZ\sigma_y - (X^2 - Y^2)\sigma_z], \tag{7}$$

where we omit the numerical coefficient and the contribution from the orbital angular momentum for simplicity; we also omit the subscript j, where $\boldsymbol{R}_j = (X_j, Y_j, Z_j)$. When the antiferromagnetic structure has a magnetic toroidal quadrupole, the system exhibits symmetric spin splitting in the electronic band structure. The functional form of symmetric spin splitting in momentum space is obtained by replacing $\boldsymbol{R}_j$ with the wave vector $\boldsymbol{k} = (k_x, k_y, k_z)$, which is given by [92]

$$T_u(\boldsymbol{k}) = 3(k_x k_x \sigma_x - k_y k_z \sigma_y), \tag{8}$$
$$T_v(\boldsymbol{k}) = -\sqrt{3}(k_z k_x \sigma_y + k_y k_z \sigma_x - k_x k_y \sigma_z), \tag{9}$$
$$T_{yz}(\boldsymbol{k}) = \sqrt{3}[-(k_y^2 - k_z^2)\sigma_x + k_x k_y \sigma_y - k_z k_x \sigma_z], \tag{10}$$
$$T_{zx}(\boldsymbol{k}) = \sqrt{3}[-k_x k_y \sigma_x - (k_z^2 - k_x^2)\sigma_y + k_y k_z \sigma_z], \tag{11}$$
$$T_{xy}(\boldsymbol{k}) = \sqrt{3}[k_z k_x \sigma_x - k_y k_z \sigma_y - (k_x^2 - k_y^2)\sigma_z], \tag{12}$$

where the subscripts u and v correspond to $3z^2 - r^2$ and $x^2 - y^2$, respectively. Such symmetric spin splitting becomes the origin of linear spin current generation when the electric field or thermal gradient is applied [53,77]. This spin-split band structure and resultant linear spin current generation occur even without the SOC.

The magnetic toroidal dipole and quadrupole appear in a simple collinear antiferromagnetic structure. To show this, we consider the collinear antiferromagnetic spin configurations in the square and triangle clusters, as shown in Figure 1, where we suppose that the antiferromagnetic spin moments point along the $\pm z$ direction. By using the expression in Equation (4) and setting $\boldsymbol{R}_{\mathrm{A}} = (-1, -1, 0)$, $\boldsymbol{R}_{\mathrm{B}} = (1, 1, 0)$, $\boldsymbol{R}_{\mathrm{C}} = (1, -1, 0)$, and $\boldsymbol{R}_{\mathrm{D}} = (-1, 1, 0)$, one finds that the antiferromagnetic structure in Figure 1a induces T_v. Meanwhile, $\boldsymbol{T} = \boldsymbol{0}$, owing to the presence of the spatial inversion symmetry. Such an emergence of T_v is intuitively understood from the distribution of the magnetic toroidal dipole on the bond. When calculating the magnetic toroidal dipole on the ij bond defined by $\boldsymbol{R}_i \times \boldsymbol{\sigma}_i + \boldsymbol{R}_j \times \boldsymbol{\sigma}_j$, one can obtain the $x^2 - y^2$-type distribution of the magnetic toroidal dipole, i.e., T_v, as shown by the purple arrows in Figure 1a. Thus, the antiferromagnetic ordering in Figure 1a leads to the symmetric spin splitting in the form of $k_x k_y \sigma_z$ for $k_z = 0$ when the lattice structure is formed by the square clusters, which results in the linear spin current generation [54].

Meanwhile, when the spin polarizations for sublattices A and C are reversed in Figure 1b, the magnetic toroidal dipole T_y becomes nonzero, whereas $T_v = 0$. Then, this type of antiferromagnetic structure does not show symmetric spin splitting in the band structure. On the other hand, this magnetic structure gives rise to the nonlinear spin Hall effect, owing to a nonzero dipole component, which is irrespective of the SOC [91].

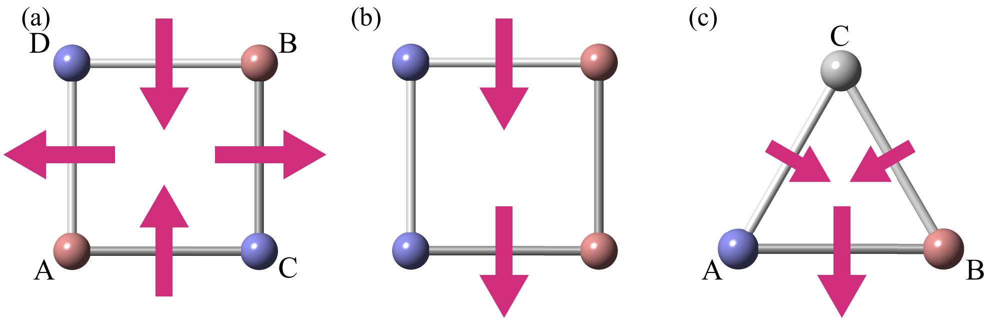

Figure 1. Schematic configurations of the spins and magnetic toroidal dipoles in (**a**,**b**) the square cluster and (**c**) the triangle cluster. The red and blue spheres represent the collinear spin moments along the z direction. The white sphere represents the zero-spin moment. The purple arrows on the bond represent the magnetic toroidal dipoles. In (**b**,**c**), the uniform component of the magnetic toroidal dipole is present.

In contrast to the square cluster, the collinear up-down-zero spin configuration in the triangle cluster induces both the magnetic toroidal dipole T_y and the magnetic toroidal quadrupole T_v, and the distribution of the magnetic toroidal dipole on the bond is shown in Figure 1c. Although the magnetic toroidal quadrupole T_u also belongs to the totally symmetric irreducible representation [93], it is not activated within the two-dimensional system. Thus, the antiferromagnetic ordering consisting of the triangle cluster exhibits both linear and nonlinear spin current generation even without the SOC. In the following, we focus on such a situation by exemplifying the breathing kagome model. We summarize the correspondence between magnetic toroidal multipoles and antiferromagnetic structures in square and triangle clusters in Table 1.

Table 1. The correspondence among the magnetic point group (MPG), induced rank-1 and rank-2 magnetic toroidal (MT) multipoles, and the emergence of the spin-split band structure (SS) and nonlinear spin Hall conductivity (NSHC) in the collinear antiferromagnets without spin–orbit coupling. ✓ in SS and NSHC stands for the presence of the spin splitting and the nonlinear spin Hall conductivity, respectively. The antiferromagnetic patterns correspond to those in Figures 1a–c from the top row. The parent point group (PG) and the irreducible representation (Irrep.) are also shown; the superscript $-$ in the Irrep. represents the odd parity with respect to the time-reversal operation.

	PG	Irrep.	MPG	MT Multipole	SS	NSHC
square	$D_{4\mathrm{h}}$	B_{1g}^{-}	$4'/mmm'$	T_v	✓	–
square	$D_{4\mathrm{h}}$	E_u^{-}	$mm'm$	T_y	–	✓
triangle	$D_{3\mathrm{h}}$	E'^{-}	$m2m$	T_y, T_v	✓	✓

2.2. Breathing Kagome Model

To investigate the spin current generation in the collinear antiferromagnetic systems with triangle clusters, we adopt the two-dimensional breathing kagome structure, whose point group symmetry is the same as the triangle cluster $D_{3\mathrm{h}}$. The breathing kagome structure consists of three sublattices A–C at $\boldsymbol{R}_\mathrm{A} = (0,0,0)$, $\boldsymbol{R}_\mathrm{B} = a(1,0,0)$, and $\boldsymbol{R}_\mathrm{C} = a(1/2,\sqrt{3}/2,0)$; we set the lattice constant $a+b$ as unity. The tight-binding Hamiltonian is given by

$$\mathcal{H} = -\Big(t\sum_{\sigma,\langle ij\rangle}^{\in\triangle} + t'\sum_{\sigma,\langle ij\rangle}^{\in\nabla}\Big)c_{i\sigma}^\dagger c_{j\sigma} - \sum_i h_i(c_{i\uparrow}^\dagger c_{i\uparrow'} - c_{i\downarrow}^\dagger c_{i\downarrow'}), \tag{13}$$

where $c_{i\sigma}^\dagger$ ($c_{i\sigma}$) is the creation (annihilation) operator at site i and spin $\sigma =\uparrow,\downarrow$. The first term represents the hoppings within upward triangles t and downward triangles t'. We set $t=1$ and $t'=0.5$ in the following calculations. The second term represents the antiferromagnetic mean-field term to induce the up-down-zero spin order: $h_{\mathrm{A}} = -h$, $h_{\mathrm{B}} = h$, and $h_{\mathrm{C}} = 0$. The schematic spin configurations in the presence of h are shown in Figure 2.

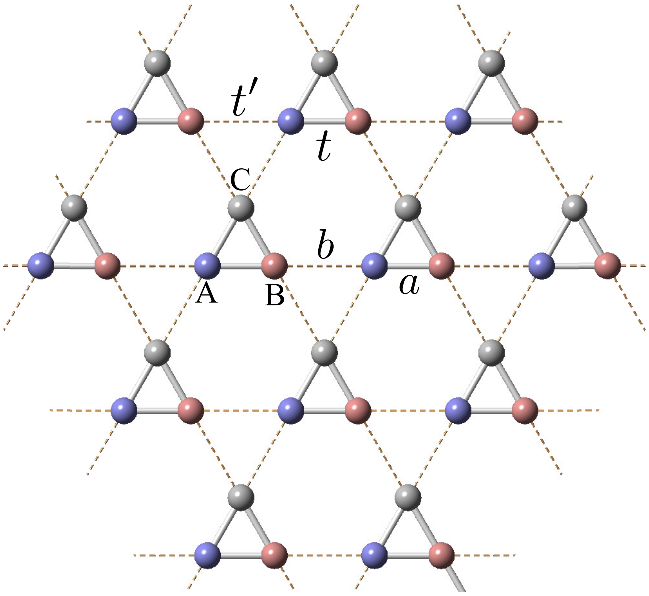

Figure 2. Two-dimensional breathing kagome structure with the lattice constant $a + b$. The red and blue spheres represent the collinear spin moments along the z direction. The white spheres represent the zero-spin moment. t and t' stand for the intra- and inter-sublattice hoppings, respectively.

3. Results

3.1. Linear Spin Conductivity

We investigate the linear spin conductivity $J^{\mathrm{s}}_{\nu} = \sum_{\mu} \sigma^{\mathrm{s}}_{\mu;\nu} E_{\mu}$ in the model in Equation (13) by using the linear response theory; $J^{\mathrm{s}}_{\nu} = J_{\nu}\sigma_z$ represents the ν-directional spin current with the z-spin component and E_{μ} represents the electric field for the $\mu = x, y$ direction. We evaluate $\sigma^{\mathrm{s}}_{\mu;\nu}$ from the $J^{\eta(\mathrm{s})}_{\nu}$–$J_{\mu}$ correlation function within the Kubo formula following Refs. [77,94] with a scattering rate $\tau^{-1} = 10^{-2}$ and a temperature $T = 10^{-2}$. The number of grid points in the Brillouin zone is $N_{\boldsymbol{k}} = 2400^2$. Nonzero tensor components in the collinear antiferromagnetic structure in Figure 2 are given by $\sigma^{\mathrm{s}}_{x;y} = \sigma^{\mathrm{s}}_{y;x}$.

Figure 3a shows $\sigma^{\mathrm{s}}_{y;x}$, while the electron filling per site n_{e} and h are varied, where $n_{\mathrm{e}} = \sum_{\boldsymbol{k}l\sigma} \langle c^{\dagger}_{\boldsymbol{k}l\sigma} c_{\boldsymbol{k}l\sigma} \rangle / (3N_{\boldsymbol{k}})$; $c^{\dagger}_{\boldsymbol{k}l\sigma}$ is the momentum–space representation of $c^{\dagger}_{i\sigma}$ at the wave vector $\boldsymbol{k}$ and the sublattice l. We also show the data at $h = 0.5$ in Figure 3b for reference. In all the regions except for $n_{\mathrm{e}} = 0$ and 2 or $h = 0$, $\sigma^{\mathrm{s}}_{y;x}$ becomes nonzero. For $\sigma^{\mathrm{s}}_{y;x}$, the intraband process is dominant, which means that $\sigma^{\mathrm{s}}_{y;x}$ is proportional to τ. This indicates that the symmetric spin splitting at the Fermi level plays an important role; $\sigma^{\mathrm{s}}_{y;x}$ tends to be enhanced for large spin splitting. We show the band structures in Figure 4a, which are plotted along the high-symmetry lines in the Brillouin zone in Figure 4b; the color map in Figure 4a represents the z-spin polarization at each wave vector. As shown in Figure 4a, the symmetric spin-split band dispersion appears in the M_2–Γ–M_3 line, while it does not in the M_1–Γ and Γ–K lines; this spin-split tendency is consistent with the functional form of $k_x k_y \sigma_z$. For $h = 0.5$, $\sigma^{\mathrm{s}}_{y;x}$ becomes larger when the Fermi level lies in the middle or top two bands in Figure 4a, where the symmetric spin splitting becomes larger than that in the bottom two bands.

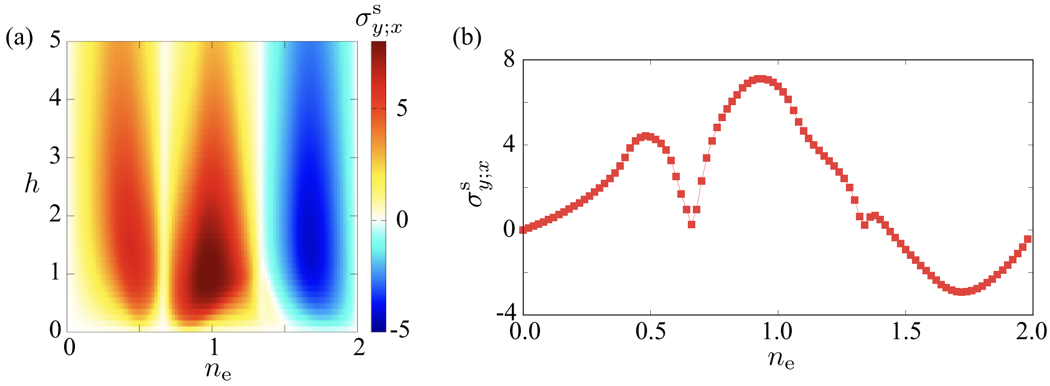

Figure 3. (**a**) Contour plot of the linear spin conductivity $\sigma^{\mathrm{s}}_{y;x}$ in the plane of the electron filling n_{e} and the molecular field h at $t = 1$ and $t' = 0.5$. (**b**) n_{e} dependence of $\sigma^{\mathrm{s}}_{y;x}$ at $h = 0.5$.

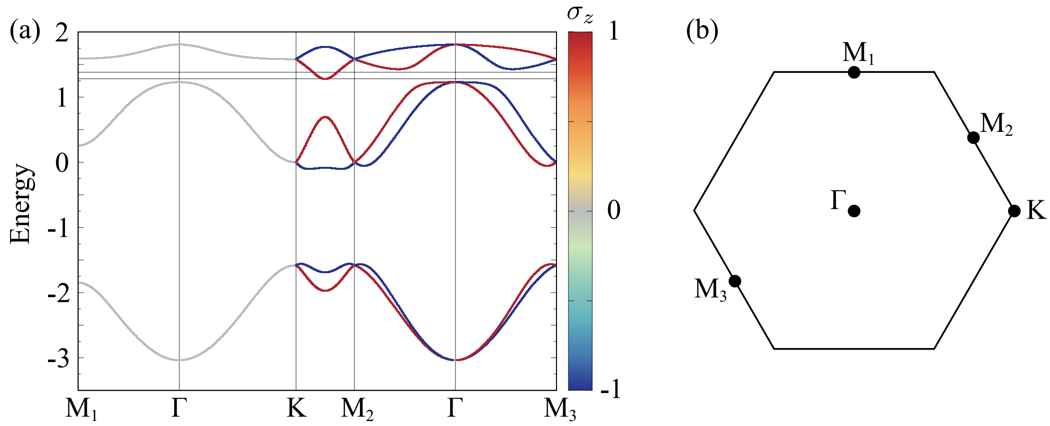

Figure 4. (**a**) Electronic band structure in the breathing kagome system under the collinear AFM structure at $t = 1$, $t' = 0.5$, and $h = 0.5$. The contour represents the spin polarization in terms of the z component, σ_z. The upper (lower) horizontal line stands for the chemical potential that maximizes (minimizes) $\sigma^{\mathrm{s}}_{y;xy}$ in Figure 5b. (**b**) The Brillouin zone in the breathing kagome system.

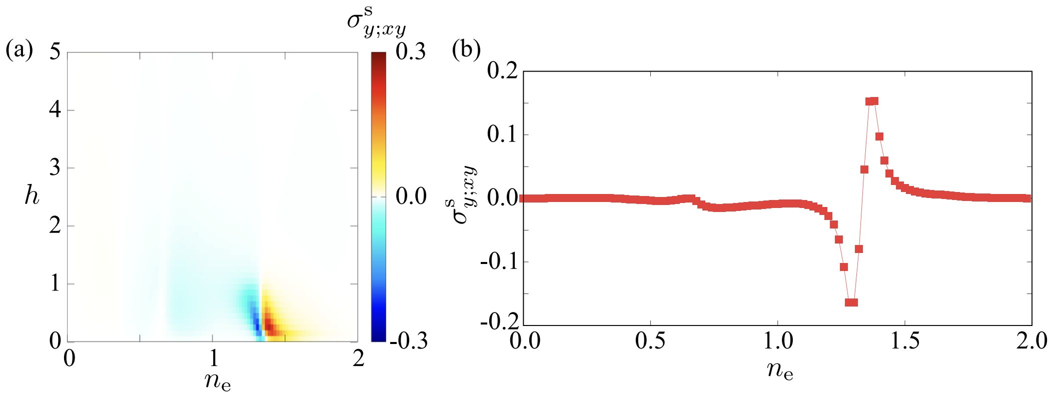

Figure 5. (**a**) Contour plot of the nonlinear spin Hall conductivity $\sigma^{\mathrm{s}}_{y;xy}$ in the plane of the electron filling n_{e} and the molecular field h at $t = 1$ and $t' = 0.5$. (**b**) n_{e} dependence of $\sigma^{\mathrm{s}}_{y;xy}$ at $h = 0.5$.

3.2. Nonlinear Spin Hall Conductivity

We calculate the nonlinear spin Hall conductivity $J^{\mathrm{s}}_{\gamma} = \sum_{\mu\nu} \sigma^{\mathrm{s}}_{\gamma;\mu\nu} E_\mu E_\nu$ by using the second-order Kubo formula with the relaxation time approximation. The specific expression is given by [91,95]

$$\sigma^{\mathrm{s}}_{\gamma;\mu\nu} = \frac{e^3\tau}{2\hbar^2 N_{\boldsymbol{k}}} \sum_{\boldsymbol{k},n} f_{n\boldsymbol{k}} \epsilon_{\gamma\mu\lambda} D^{\nu\lambda(\mathrm{s})}_{n}(\boldsymbol{k}) + (\mu \leftrightarrow \nu), \tag{14}$$

where $\epsilon_{\eta\mu\lambda}$ represents the Levi–Civita tensor. We take the electric charge e, the reduced Planck constant $\hbar$, and the relaxation time τ as unity, i.e., $e = \hbar = \tau = 1$. $f_{n\boldsymbol{k}}$ is the Fermi distribution function with the band index n, and $D_n^{\mu\nu(\mathrm{s})}(\boldsymbol{k})$ denotes the spin-dependent Berry curvature dipole, which is related to the spin-dependent Berry curvature $\Omega_n^{\nu(\mathrm{s})}(\boldsymbol{k})$ as $D_n^{\mu\nu(\mathrm{s})}(\boldsymbol{k}) = \partial_\mu \Omega_n^{\nu(\mathrm{s})}(\boldsymbol{k})$ [95,96]. In the case of the collinear antiferromagnetic structure in Figure 2, the nonzero tensor components of $\sigma^{\mathrm{s}}_{\gamma;\mu\nu}$ are given by $\sigma^{z(\mathrm{s})}_{x;yy} = -2\sigma^{z(\mathrm{s})}_{y;xy}$. In contrast to the noncentrosymmetric systems with the relativistic SOC [97–101], the present mechanism is driven by magnetic order, which does not require the SOC.

Figure 5a shows the behavior of $\sigma^{\mathrm{s}}_{y;xy}$ in the plane of n_{e} and h. Similar to the linear spin conductivity $\sigma^{\mathrm{s}}_{y;x}$, $\sigma^{\mathrm{s}}_{y;xy}$ becomes nonzero except for $n_{\mathrm{e}} = 0$ and 2 or $h = 0$, although almost all of the regions except around the area with $1.3 \lesssim n_{\mathrm{e}} \lesssim 1.5$ and $0 < h \lesssim 1$ take small values. We show the n_{e} dependence of $\sigma^{\mathrm{s}}_{y;xy}$ at $h = 0.5$ in Figure 5b, where $\sigma^{\mathrm{s}}_{y;xy}$ takes the minimum and maximum values at $n_{\mathrm{e}} \simeq 1.28$ and 1.38, respectively.

The enhancement of $\sigma^{\mathrm{s}}_{y;xy}$ in the specific region is understood from the fact that both intraband and interband processes contribute to $\sigma^{\mathrm{s}}_{y;xy}$. Since the interband process also contributes to $\sigma^{\mathrm{s}}_{y;xy}$, the small band gap leading to the small energy denominator included in the spin-dependent Berry curvature dipole is important. Indeed, one finds that the small band gap appears close to the Fermi level, as shown by the band structure in Figure 4a; the upper (lower) horizontal line represents the chemical potential that gives the maximum (minimum) of $\sigma^{\mathrm{s}}_{y;xy}$.

4. Discussion

Finally, let us compare the behavior of the linear spin conductivity $\sigma^{\mathrm{s}}_{y;x}$ and nonlinear spin Hall conductivity $\sigma^{\mathrm{s}}_{y;xy}$ in the collinear antiferromagnets with triangle clusters. Although their relaxation time dependence proportional to τ is the same, their symmetry and microscopic conditions are different from each other; the linear spin conductivity appears when the magnetic toroidal quadrupole is activated, while the nonlinear spin Hall conductivity appears when the magnetic toroidal dipole is activated. Reflecting such a difference, the linear spin conductivity is dominated by the intraband process originating from the symmetric spin-split band structure, while the nonlinear spin conductivity is relevant to both intraband and interband processes and is not relevant to the symmetric spin splitting. Accordingly, the model parameter dependence is different, as shown in Figures 3a and 5a, where the linear spin conductivity tends to be larger than the nonlinear spin conductivity.

Meanwhile, the nonlinear spin conductivity becomes larger than the linear spin conductivity when the Fermi level is located near the band gap. Figure 6a shows the ratio of two spin conductivities, $R = \sigma^{\mathrm{s}}_{y;xy}/\sigma^{\mathrm{s}}_{y;x}$, in the plane of n_{e} and h, where $\tau^{-1} = 10^{-2}$ is taken for both conductivities. We also show the absolute value $|R|$ for different contour ranges in Figure 6b for reference. In the region where the nonlinear spin conductivity is enhanced for $1.3 \lesssim n_{\mathrm{e}} \lesssim 1.5$ and $0 < h \lesssim 1$, the nonlinear spin conductivity can have a comparable contribution to the linear one. In other words, the contribution from nonlinear spin conductivity is non-negligible depending on the chemical potential.

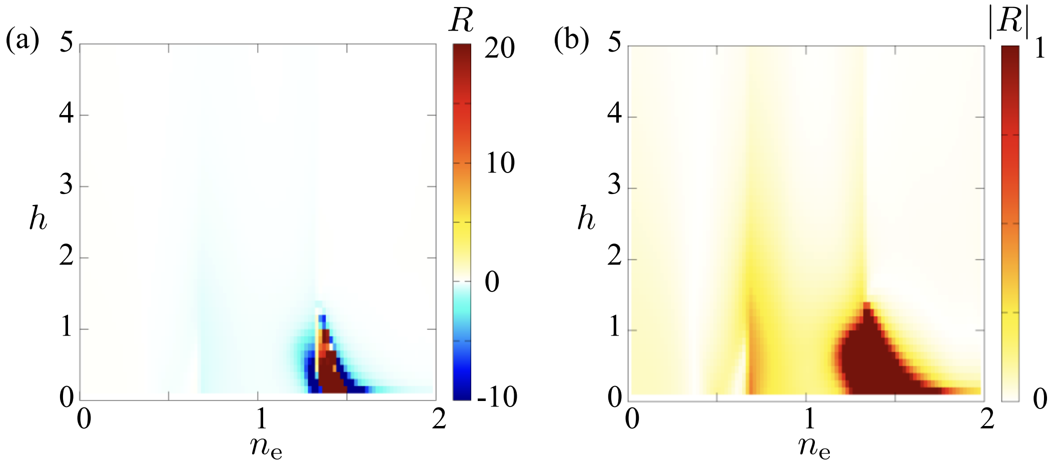

Figure 6. (**a**) n_e and h dependence of the ratio $R = \sigma^{s}_{y;xy}/\sigma^{s}_{y;x}$ at $t = 1$, $t' = 0.5$, and $\tau^{-1} = 0.01$. (**b**) Enlarged figure of (**a**) for $0 \leq |R| \leq 1$.

5. Conclusions

In conclusion, we investigated the spin current generation in collinear antiferromagnets without the relativistic SOC. By focusing on the difference in the cluster geometry, we have shown that the collinear antiferromagnetic spin configuration in the triangle cluster gives rise to qualitatively different transport phenomena from those in the square cluster. In the case of the square cluster, either linear spin conductivity or nonlinear spin conductivity is induced depending on the type of antiferromagnetic spin configuration, while both spin conductivities occur in the up-down-zero spin configuration in the case of the triangle cluster. We have demonstrated the emergence of linear and nonlinear spin conductivities by examining the two-dimensional breathing kagome structure consisting of the triangle clusters. When the Fermi level lies near the band gap, the contribution from the nonlinear spin conductivity is comparable to that from the linear spin conductivity. Our results indicate that the different cluster geometry gives rise to different behaviors of spin conductivity in SOC-free antiferromagnets, whose difference would be utilized for future spintronics applications.

Funding: This research was supported by JSPS KAKENHI Grant Numbers JP21H01037, JP22H00101, JP22H01183, JP23H04869, JP23K03288, JP23K20827, and by JST CREST (JPMJCR23O4).

Data Availability Statement: The data presented in this study are available on request from the corresponding author.

Conflicts of Interest: The author declares no conflicts of interest.

References

1. Diep, H.T. *Frustrated Spin Systems*; World Scientific: Singapore, 2004.
2. Lacroix, C.; Mendels, P.; Mila, F., Eds. *Introduction to Frustrated Magnetism: Materials, Experiments, Theory*; Springer Series in Solid-State Sciences; Springer: Berlin/Heidelberg, Germany, 2011.
3. Bulaevskii, L.N.; Batista, C.D.; Mostovoy, M.V.; Khomskii, D.I. Electronic orbital currents and polarization in Mott insulators. *Phys. Rev. B* **2008**, *78*, 024402. [CrossRef]
4. Hayami, S.; Kusunose, H. Unified Description of Electronic Orderings and Cross Correlations by Complete Multipole Representation. *J. Phys. Soc. Jpn.* **2024**, *93*, 072001. [CrossRef]
5. Kimura, T.; Goto, T.; Shintani, H.; Ishizaka, K.; Arima, T.; Tokura, Y. Magnetic control of ferroelectric polarization. *Nature* **2003**, *426*, 55–58. [CrossRef] [PubMed]
6. Fiebig, M. Revival of the magnetoelectric effect. *J. Phys. D Appl. Phys.* **2005**, *38*, R123. [CrossRef]
7. Spaldin, N.A.; Fiebig, M. The renaissance of magnetoelectric multiferroics. *Science* **2005**, *309*, 391–392. [CrossRef] [PubMed]
8. Ramesh, R.; Spaldin, N.A. Multiferroics: Progress and prospects in thin films. *Nat. Mater.* **2007**, *6*, 21. [CrossRef]
9. Khomskii, D. Classifying multiferroics: Mechanisms and effects. *Physics* **2009**, *2*, 20. [CrossRef]
10. Tokura, Y.; Seki, S.; Nagaosa, N. Multiferroics of spin origin. *Rep. Prog. Phys.* **2014**, *77*, 076501. [CrossRef]
11. Fiebig, M.; Lottermoser, T.; Meier, D.; Trassin, M. The evolution of multiferroics. *Nat. Rev. Mater.* **2016**, *1*, 16046. [CrossRef]

12. Ohgushi, K.; Murakami, S.; Nagaosa, N. Spin anisotropy and quantum Hall effect in the *kagomé* lattice: Chiral spin state based on a ferromagnet. *Phys. Rev. B* **2000**, *62*, R6065–R6068. [CrossRef]
13. Shindou, R.; Nagaosa, N. Orbital Ferromagnetism and Anomalous Hall Effect in Antiferromagnets on the Distorted fcc Lattice. *Phys. Rev. Lett.* **2001**, *87*, 116801. [CrossRef] [PubMed]
14. Neubauer, A.; Pfleiderer, C.; Binz, B.; Rosch, A.; Ritz, R.; Niklowitz, P.G.; Böni, P. Topological Hall Effect in the *A* Phase of MnSi. *Phys. Rev. Lett.* **2009**, *102*, 186602. [CrossRef] [PubMed]
15. Nagaosa, N.; Sinova, J.; Onoda, S.; MacDonald, A.H.; Ong, N.P. Anomalous Hall effect. *Rev. Mod. Phys.* **2010**, *82*, 1539–1592. [CrossRef]
16. Xiao, D.; Chang, M.C.; Niu, Q. Berry phase effects on electronic properties. *Rev. Mod. Phys.* **2010**, *82*, 1959–2007. [CrossRef]
17. Chen, H.; Niu, Q.; MacDonald, A.H. Anomalous Hall Effect Arising from Noncollinear Antiferromagnetism. *Phys. Rev. Lett.* **2014**, *112*, 017205. [CrossRef]
18. Nakatsuji, S.; Kiyohara, N.; Higo, T. Large anomalous Hall effect in a non-collinear antiferromagnet at room temperature. *Nature* **2015**, *527*, 212. [CrossRef] [PubMed]
19. Suzuki, M.T.; Koretsune, T.; Ochi, M.; Arita, R. Cluster multipole theory for anomalous Hall effect in antiferromagnets. *Phys. Rev. B* **2017**, *95*, 094406. [CrossRef]
20. Chen, H.; Wang, T.C.; Xiao, D.; Guo, G.Y.; Niu, Q.; MacDonald, A.H. Manipulating anomalous Hall antiferromagnets with magnetic fields. *Phys. Rev. B* **2020**, *101*, 104418. [CrossRef]
21. Feng, W.; Hanke, J.P.; Zhou, X.; Guo, G.Y.; Blügel, S.; Mokrousov, Y.; Yao, Y. Topological magneto-optical effects and their quantization in noncoplanar antiferromagnets. *Nat. Commun.* **2020**, *11*, 118. [CrossRef]
22. Yanase, Y. Magneto-Electric Effect in Three-Dimensional Coupled Zigzag Chains. *J. Phys. Soc. Jpn.* **2014**, *83*, 014703. [CrossRef]
23. Hayami, S.; Kusunose, H.; Motome, Y. Spontaneous Multipole Ordering by Local Parity Mixing. *J. Phys. Soc. Jpn.* **2015**, *84*, 064717. [CrossRef]
24. Sumita, S.; Yanase, Y. Superconductivity in magnetic multipole states. *Phys. Rev. B* **2016**, *93*, 224507. [CrossRef]
25. Matsumura, T.; Yamamoto, T.; Tanida, H.; Sera, M. Temperature-Dependent Cycloidal Magnetic Structure in $GdRu_2Al_{10}$ Studied by Resonant X-ray Diffraction. *J. Phys. Soc. Jpn.* **2017**, *86*, 094709. [CrossRef]
26. Cysne, T.P.; Guimarães, F.S.M.; Canonico, L.M.; Rappoport, T.G.; Muniz, R.B. Orbital magnetoelectric effect in zigzag nanoribbons of *p*-band systems. *Phys. Rev. B* **2021**, *104*, 165403. [CrossRef]
27. Yatsushiro, M.; Oiwa, R.; Kusunose, H.; Hayami, S. Analysis of model-parameter dependences on the second-order nonlinear conductivity in $\mathcal{PT}$-symmetric collinear antiferromagnetic metals with magnetic toroidal moment on zigzag chains. *Phys. Rev. B* **2022**, *105*, 155157. [CrossRef]
28. Suzuki, Y. Tunneling spin current in systems with spin degeneracy. *Phys. Rev. B* **2022**, *105*, 075201. [CrossRef]
29. Li, D.X.; Honda, F.; Miyake, A.; Homma, Y.; Haga, Y.; Nakamura, A.; Shimizu, Y.; Maurya, A.; Sato, Y.J.; Tokunaga, M.; et al. Magnetic and electrical properties of the ternary compound $U_2Ir_3Si_5$ with one-dimensional uranium zigzag chains. *Phys. Rev. B* **2019**, *99*, 054408. [CrossRef]
30. Li, X.; Cao, T.; Niu, Q.; Shi, J.; Feng, J. Coupling the valley degree of freedom to antiferromagnetic order. *Proc. Natl. Acad. Sci. USA* **2013**, *110*, 3738–3742. [CrossRef]
31. Hayami, S.; Kusunose, H.; Motome, Y. Spontaneous parity breaking in spin-orbital coupled systems. *Phys. Rev. B* **2014**, *90*, 081115. [CrossRef]
32. Hayami, S.; Kusunose, H.; Motome, Y. Emergent spin-valley-orbital physics by spontaneous parity breaking. *J. Phys. Condens. Matter* **2016**, *28*, 395601. [CrossRef]
33. Yanagi, Y.; Kusunose, H. Optical Selection Rules in Spin–Orbit Coupled Systems on Honeycomb Lattice. *J. Phys. Soc. Jpn.* **2017**, *86*, 083703. [CrossRef]
34. Oishi, R.; Umeo, K.; Shimura, Y.; Onimaru, T.; Strydom, A.M.; Takabatake, T. Antiferromagnetic order in the honeycomb Kondo lattice $CePt_6Al_3$ induced by Pd substitution. *Phys. Rev. B* **2021**, *104*, 104411. [CrossRef]
35. Hayami, S.; Kusunose, H.; Motome, Y. Emergent odd-parity multipoles and magnetoelectric effects on a diamond structure: Implication for the 5*d* transition metal oxides $A\mathrm{OsO}_4$ $(A = \mathrm{K}, \mathrm{Rb}, \text{and Cs})$. *Phys. Rev. B* **2018**, *97*, 024414. [CrossRef]
36. Ishitobi, T.; Hattori, K. Magnetoelectric Effects and Charge-Imbalanced Solenoids: Antiferro Quadrupole Orders in a Diamond Structure. *J. Phys. Soc. Jpn.* **2019**, *88*, 063708. [CrossRef]
37. Yamaura, J.i.; Hiroi, Z. Crystal structure and magnetic properties of the 5*d* transition metal oxides $A\mathrm{OsO}_4(A = \mathrm{K},\ \mathrm{Rb},\ \mathrm{Cs})$. *Phys. Rev. B* **2019**, *99*, 155113. [CrossRef]
38. Paramekanti, A.; Maharaj, D.D.; Gaulin, B.D. Octupolar order in *d*-orbital Mott insulators. *Phys. Rev. B* **2020**, *101*, 054439. [CrossRef]
39. Maharaj, D.D.; Sala, G.; Stone, M.B.; Kermarrec, E.; Ritter, C.; Fauth, F.; Marjerrison, C.A.; Greedan, J.E.; Paramekanti, A.; Gaulin, B.D. Octupolar versus Néel Order in Cubic $5d^2$ Double Perovskites. *Phys. Rev. Lett.* **2020**, *124*, 087206. [CrossRef]
40. Winkler, R.; Zülicke, U. Theory of electric, magnetic, and toroidal polarizations in crystalline solids with applications to hexagonal lonsdaleite and cubic diamond. *Phys. Rev. B* **2023**, *107*, 155201. [CrossRef]
41. Solovyev, I.V. Magneto-optical effect in the weak ferromagnets $LaMO_3$ (M= Cr, Mn, and Fe). *Phys. Rev. B* **1997**, *55*, 8060–8063. [CrossRef]

42. Sivadas, N.; Okamoto, S.; Xiao, D. Gate-Controllable Magneto-optic Kerr Effect in Layered Collinear Antiferromagnets. *Phys. Rev. Lett.* **2016**, *117*, 267203. [CrossRef]
43. Yamasaki, Y.; Nakao, H.; Arima, T.h. Augmented Magnetic Octupole in Kagomé 120-degree Antiferromagnets Detectable via X-ray Magnetic Circular Dichroism. *J. Phys. Soc. Jpn.* **2020**, *89*, 083703. [CrossRef]
44. Šmejkal, L.; González-Hernández, R.; Jungwirth, T.; Sinova, J. Crystal time-reversal symmetry breaking and spontaneous Hall effect in collinear antiferromagnets. *Sci. Adv.* **2020**, *6*, eaaz8809. [CrossRef] [PubMed]
45. Naka, M.; Hayami, S.; Kusunose, H.; Yanagi, Y.; Motome, Y.; Seo, H. Anomalous Hall effect in κ-type organic antiferromagnets. *Phys. Rev. B* **2020**, *102*, 075112. [CrossRef]
46. Hayami, S.; Kusunose, H. Essential role of the anisotropic magnetic dipole in the anomalous Hall effect. *Phys. Rev. B* **2021**, *103*, L180407. [CrossRef]
47. Kimata, M.; Sasabe, N.; Kurita, K.; Yamasaki, Y.; Tabata, C.; Yokoyama, Y.; Kotani, Y.; Ikhlas, M.; Tomita, T.; Amemiya, K.; et al. X-ray study of ferroic octupole order producing anomalous Hall effect. *Nat. Commun.* **2021**, *12*, 5582. [CrossRef] [PubMed]
48. Chen, H. Electronic chiralization as an indicator of the anomalous Hall effect in unconventional magnetic systems. *Phys. Rev. B* **2022**, *106*, 024421. [CrossRef]
49. Sasabe, N.; Kimata, M.; Nakamura, T. Presence of X-Ray Magnetic Circular Dichroism Signal for Zero-Magnetization Antiferromagnetic State. *Phys. Rev. Lett.* **2021**, *126*, 157402. [CrossRef]
50. Noda, Y.; Ohno, K.; Nakamura, S. Momentum-dependent band spin splitting in semiconducting MnO 2: A density functional calculation. *Phys. Chem. Chem. Phys.* **2016**, *18*, 13294–13303. [CrossRef] [PubMed]
51. Okugawa, T.; Ohno, K.; Noda, Y.; Nakamura, S. Weakly spin-dependent band structures of antiferromagnetic perovskite LaMO3 (M= Cr, Mn, Fe). *J. Phys. Condens. Matter* **2018**, *30*, 075502. [CrossRef]
52. Ahn, K.H.; Hariki, A.; Lee, K.W.; Kuneš, J. Antiferromagnetism in RuO_2 as *d*-wave Pomeranchuk instability. *Phys. Rev. B* **2019**, *99*, 184432. [CrossRef]
53. Naka, M.; Hayami, S.; Kusunose, H.; Yanagi, Y.; Motome, Y.; Seo, H. Spin current generation in organic antiferromagnets. *Nat. Commun.* **2019**, *10*, 4305. [CrossRef] [PubMed]
54. Hayami, S.; Yanagi, Y.; Kusunose, H. Momentum-Dependent Spin Splitting by Collinear Antiferromagnetic Ordering. *J. Phys. Soc. Jpn.* **2019**, *88*, 123702. [CrossRef]
55. Hayami, S.; Yanagi, Y.; Kusunose, H. Spontaneous antisymmetric spin splitting in noncollinear antiferromagnets without spin-orbit coupling. *Phys. Rev. B* **2020**, *101*, 220403(R). [CrossRef]
56. Hayami, S.; Yanagi, Y.; Kusunose, H. Bottom-up design of spin-split and reshaped electronic band structures in antiferromagnets without spin-orbit coupling: Procedure on the basis of augmented multipoles. *Phys. Rev. B* **2020**, *102*, 144441. [CrossRef]
57. Yuan, L.D.; Wang, Z.; Luo, J.W.; Rashba, E.I.; Zunger, A. Giant momentum-dependent spin splitting in centrosymmetric low-Z antiferromagnets. *Phys. Rev. B* **2020**, *102*, 014422. [CrossRef]
58. Egorov, S.A.; Evarestov, R.A. Colossal Spin Splitting in the Monolayer of the Collinear Antiferromagnet MnF2. *J. Phys. Chem. Lett.* **2021**, *12*, 2363–2369. [CrossRef]
59. Yuan, L.D.; Wang, Z.; Luo, J.W.; Zunger, A. Strong influence of nonmagnetic ligands on the momentum-dependent spin splitting in antiferromagnets. *Phys. Rev. B* **2021**, *103*, 224410. [CrossRef]
60. Yuan, L.D.; Wang, Z.; Luo, J.W.; Zunger, A. Prediction of low-Z collinear and noncollinear antiferromagnetic compounds having momentum-dependent spin splitting even without spin-orbit coupling. *Phys. Rev. Mater.* **2021**, *5*, 014409. [CrossRef]
61. Mazin, I.I. Altermagnetism in MnTe: Origin, predicted manifestations, and routes to detwinning. *Phys. Rev. B* **2023**, *107*, L100418. [CrossRef]
62. Lovesey, S.W.; Khalyavin, D.D.; van der Laan, G. Templates for magnetic symmetry and altermagnetism in hexagonal MnTe. *Phys. Rev. B* **2023**, *108*, 174437. [CrossRef]
63. Yuan, L.D.; Zunger, A. Degeneracy Removal of Spin Bands in Collinear Antiferromagnets with Non-Interconvertible Spin-Structure Motif Pair. *Adv. Mater.* **2023**, *35*, 2211966. [CrossRef] [PubMed]
64. Yuan, L.D.; Zhang, X.; Acosta, C.M.; Zunger, A. Uncovering spin-orbit coupling-independent hidden spin polarization of energy bands in antiferromagnets. *Nat. Commun.* **2023**, *14*, 5301. [CrossRef]
65. Gonzalez Betancourt, R.D.; Zubáč, J.; Gonzalez-Hernandez, R.; Geishendorf, K.; Šobáň, Z.; Springholz, G.; Olejník, K.; Šmejkal, L.; Sinova, J.; Jungwirth, T.; et al. Spontaneous Anomalous Hall Effect Arising from an Unconventional Compensated Magnetic Phase in a Semiconductor. *Phys. Rev. Lett.* **2023**, *130*, 036702. [CrossRef] [PubMed]
66. Ouassou, J.A.; Brataas, A.; Linder, J. dc Josephson Effect in Altermagnets. *Phys. Rev. Lett.* **2023**, *131*, 076003. [CrossRef]
67. Cui, Q.; Zeng, B.; Cui, P.; Yu, T.; Yang, H. Efficient spin Seebeck and spin Nernst effects of magnons in altermagnets. *Phys. Rev. B* **2023**, *108*, L180401. [CrossRef]
68. Brekke, B.; Brataas, A.; Sudbø, A. Two-dimensional altermagnets: Superconductivity in a minimal microscopic model. *Phys. Rev. B* **2023**, *108*, 224421. [CrossRef]
69. Aoyama, T.; Ohgushi, K. Piezomagnetic properties in altermagnetic MnTe. *Phys. Rev. Mater.* **2024**, *8*, L041402. [CrossRef]
70. Hariki, A.; Takahashi, Y.; Kuneš, J. X-ray magnetic circular dichroism in RuO_2. *Phys. Rev. B* **2024**, *109*, 094413. [CrossRef]
71. Osumi, T.; Souma, S.; Aoyama, T.; Yamauchi, K.; Honma, A.; Nakayama, K.; Takahashi, T.; Ohgushi, K.; Sato, T. Observation of a giant band splitting in altermagnetic MnTe. *Phys. Rev. B* **2024**, *109*, 115102. [CrossRef]

72. Hariki, A.; Dal Din, A.; Amin, O.J.; Yamaguchi, T.; Badura, A.; Kriegner, D.; Edmonds, K.W.; Campion, R.P.; Wadley, P.; Backes, D.; et al. X-Ray Magnetic Circular Dichroism in Altermagnetic α-MnTe. *Phys. Rev. Lett.* **2024**, *132*, 176701. [CrossRef]
73. Šmejkal, L.; Sinova, J.; Jungwirth, T. Beyond Conventional Ferromagnetism and Antiferromagnetism: A Phase with Nonrelativistic Spin and Crystal Rotation Symmetry. *Phys. Rev. X* **2022**, *12*, 031042. [CrossRef]
74. Šmejkal, L.; Sinova, J.; Jungwirth, T. Emerging Research Landscape of Altermagnetism. *Phys. Rev. X* **2022**, *12*, 040501. [CrossRef]
75. Shao, D.F.; Zhang, S.H.; Li, M.; Eom, C.B.; Tsymbal, E.Y. Spin-neutral currents for spintronics. *Nat. Commun.* **2021**, *12*, 7061. [CrossRef] [PubMed]
76. González-Hernández, R.; Šmejkal, L.; Výborný, K.; Yahagi, Y.; Sinova, J.; Jungwirth, T.; Železný, J. Efficient Electrical Spin Splitter Based on Nonrelativistic Collinear Antiferromagnetism. *Phys. Rev. Lett.* **2021**, *126*, 127701. [CrossRef] [PubMed]
77. Hayami, S.; Yatsushiro, M. Spin Conductivity Based on Magnetic Toroidal Quadrupole Hidden in Antiferromagnets. *J. Phys. Soc. Jpn.* **2022**, *91*, 063702. [CrossRef]
78. Bai, H.; Zhang, Y.C.; Zhou, Y.J.; Chen, P.; Wan, C.H.; Han, L.; Zhu, W.X.; Liang, S.X.; Su, Y.C.; Han, X.F.; et al. Efficient Spin-to-Charge Conversion via Altermagnetic Spin Splitting Effect in Antiferromagnet RuO_2. *Phys. Rev. Lett.* **2023**, *130*, 216701. [CrossRef] [PubMed]
79. Spaldin, N.A.; Fiebig, M.; Mostovoy, M. The toroidal moment in condensed-matter physics and its relation to the magnetoelectric effect. *J. Phys. Condens. Matter* **2008**, *20*, 434203. [CrossRef]
80. Kopaev, Y.V. Toroidal ordering in crystals. *Physics-Uspekhi* **2009**, *52*, 1111–1125. [CrossRef]
81. Hayami, S.; Kusunose, H. Microscopic Description of Electric and Magnetic Toroidal Multipoles in Hybrid Orbitals. *J. Phys. Soc. Jpn.* **2018**, *87*, 033709. [CrossRef]
82. Suzuki, M.T.; Nomoto, T.; Arita, R.; Yanagi, Y.; Hayami, S.; Kusunose, H. Multipole expansion for magnetic structures: A generation scheme for a symmetry-adapted orthonormal basis set in the crystallographic point group. *Phys. Rev. B* **2019**, *99*, 174407. [CrossRef]
83. Popov, Y.F.; Kadomtseva, A.; Belov, D.; Vorob'ev, G.; Zvezdin, A. Magnetic-field-induced toroidal moment in the magnetoelectric Cr2O3. *J. Exp. Theor. Phys. Lett.* **1999**, *69*, 330–335. [CrossRef]
84. Schmid, H. On ferrotoroidics and electrotoroidic, magnetotoroidic and piezotoroidic effects*. *Ferroelectrics* **2001**, *252*, 41–50. [CrossRef]
85. Ederer, C.; Spaldin, N.A. Towards a microscopic theory of toroidal moments in bulk periodic crystals. *Phys. Rev. B* **2007**, *76*, 214404. [CrossRef]
86. Thöle, F.; Spaldin, N.A. Magnetoelectric multipoles in metals. *Philos. Trans. R. Soc. A* **2018**, *376*, 20170450. [CrossRef] [PubMed]
87. Sawada, K.; Nagaosa, N. Optical Magnetoelectric Effect in Multiferroic Materials: Evidence for a Lorentz Force Acting on a Ray of Light. *Phys. Rev. Lett.* **2005**, *95*, 237402. [CrossRef]
88. Miyahara, S.; Furukawa, N. Nonreciprocal Directional Dichroism and Toroidalmagnons in Helical Magnets. *J. Phys. Soc. Jpn.* **2012**, *81*, 023712. [CrossRef]
89. Miyahara, S.; Furukawa, N. Theory of magneto-optical effects in helical multiferroic materials via toroidal magnon excitation. *Phys. Rev. B* **2014**, *89*, 195145. [CrossRef]
90. Hayami, S.; Kusunose, H.; Motome, Y. Asymmetric Magnon Excitation by Spontaneous Toroidal Ordering. *J. Phys. Soc. Jpn.* **2016**, *85*, 053705. [CrossRef]
91. Hayami, S.; Yatsushiro, M.; Kusunose, H. Nonlinear spin Hall effect in $\mathcal{PT}$-symmetric collinear magnets. *Phys. Rev. B* **2022**, *106*, 024405. [CrossRef]
92. Hayami, S.; Yatsushiro, M.; Yanagi, Y.; Kusunose, H. Classification of atomic-scale multipoles under crystallographic point groups and application to linear response tensors. *Phys. Rev. B* **2018**, *98*, 165110. [CrossRef]
93. Yatsushiro, M.; Kusunose, H.; Hayami, S. Multipole classification in 122 magnetic point groups for unified understanding of multiferroic responses and transport phenomena. *Phys. Rev. B* **2021**, *104*, 054412. [CrossRef]
94. Mook, A.; Neumann, R.R.; Johansson, A.; Henk, J.; Mertig, I. Origin of the magnetic spin Hall effect: Spin current vorticity in the Fermi sea. *Phys. Rev. Res.* **2020**, *2*, 023065. [CrossRef]
95. Sodemann, I.; Fu, L. Quantum Nonlinear Hall Effect Induced by Berry Curvature Dipole in Time-Reversal Invariant Materials. *Phys. Rev. Lett.* **2015**, *115*, 216806. [CrossRef] [PubMed]
96. Kondo, H.; Akagi, Y. Nonlinear magnon spin Nernst effect in antiferromagnets and strain-tunable pure spin current. *Phys. Rev. Res.* **2022**, *4*, 013186. [CrossRef]
97. Yu, H.; Wu, Y.; Liu, G.B.; Xu, X.; Yao, W. Nonlinear Valley and Spin Currents from Fermi Pocket Anisotropy in 2D Crystals. *Phys. Rev. Lett.* **2014**, *113*, 156603. [CrossRef]
98. Hamamoto, K.; Ezawa, M.; Kim, K.W.; Morimoto, T.; Nagaosa, N. Nonlinear spin current generation in noncentrosymmetric spin-orbit coupled systems. *Phys. Rev. B* **2017**, *95*, 224430. [CrossRef]
99. Araki, Y. Strain-induced nonlinear spin Hall effect in topological Dirac semimetal. *Sci. Rep.* **2018**, *8*, 15236. [CrossRef]

100. Pan, A.; Marinescu, D.C. Nonlinear spin-current generation in quantum wells with arbitrary Rashba-Dresselhaus spin-orbit interactions. *Phys. Rev. B* **2019**, *99*, 245204. [CrossRef]
101. Zhang, Z.F.; Zhu, Z.G.; Su, G. Theory of nonlinear response for charge and spin currents. *Phys. Rev. B* **2021**, *104*, 115140. [CrossRef]